Development of a two-dimensional virtual-pixel X-ray imaging detector for time-resolved structure research

Andre Orthen,[a]* Hendrik Wagner,[a] Sorin Martoiu,[a] Heinz Amenitsch,[b] Sigrid Bernstorff,[c] Hans-Jürgen Besch,[a] Ralf-Hendrik Menk,[c] Kivanç Nurdan,[a] Michael Rappolt,[b] Albert Heinrich Walenta[a] and Ulrich Werthenbach[a]

[a]Universität Siegen, Fachbereich Physik, Emmy-Noether-Campus, Walter-Flex-Straße 3, D-57072 Siegen, Germany, [b]Institute of Biophysics and X-ray Structure Research, Austrian Academy of Sciences, Schmiedlstraße 6, A-8042 Graz, Austria, and [c]Sincrotrone Trieste, SS 14, Km 163.5, Basovizza, I-34012 Trieste, Italy. E-mail: orthen@alwa02.physik.uni-siegen.de

An interpolating two-dimensional X-ray imaging detector based on a single-photon counter with gas amplification by GEM (gas electron multiplier) structures is presented. The detector system can be used for time-resolved structure research down to the µs time domain. The prototype detector has been tested at the SAXS (small-angle X-ray scattering) beamline at ELETTRA synchrotron light source with a beam energy of 8 keV. The imaging performance is examined with apertures and standard diffraction targets. Finally, the application in a time-resolved lipid temperature-jump experiment is presented.

Keywords: micropattern gaseous detectors; time-resolved X-ray imaging; two-dimensional detectors; small-angle X-ray scattering; lipid phase transitions.

1. Introduction

Modern synchrotron radiation facilities are able to provide extremely high photon fluxes with an enormous brilliance, which opens up new research fields in many different areas. One of these branches is the study of fast time-resolved processes. Of special interest are, for example, dynamical processes in material science (Clery, 1997), such as phase transitions, polymerization or deformations under stress. In the chemical or biological domain, for example, muscle contraction (Squire *et al.*, 1991; Wakabayashi & Amemiya, 1991; Holmes & Geeves, 2000; Piazzesi *et al.*, 2002) or lipid phase transitions (Rapp, 1991; Seddon & Templer, 1995) come into the focus of interest.

The existing X-ray detectors, however, do not offer the time resolutions needed or are often not capable of dealing with the enormous photon rates produced by insertion devices like wigglers, undulators or in the future by free-electron lasers, and are the bottleneck of state-of-the-art beamlines. To find a solution for this mismatch, one has to improve old detector concepts or introduce new approaches.

Detectors in general can be classified into two categories: integrating detectors and single-photon counters. The performance of integrating devices like CCDs (charge coupled devices), image plates or X-ray films is becoming more favourable at high photon flux, since the relative noise contribution is decreasing. The noise contributions can be attributed to noise caused by fluctuations of the measured quantity related to the input (intrinsic noise), to dark noise and to readout noise. The readout noise increases in proportion to the readout frame rate, whereby in most CCDs this noise contribution is much larger than the dark noise. Time resolution is thus competing with intensity precision; generally, the time resolution is limited to keep the readout noise contribution relatively small. At some value of input flux the integrator saturates and cannot add up more until the content is reset. The dynamic range of integrating devices, which is typically 10^4–10^5, is thus limited by noise and saturation level.

In contrast to integrating devices, counting detectors like MWPCs (multiwire proportional chambers) or MSGCs (microstrip gas chambers) are not sensitive to noise contributions, described above, as long as this noise level is below the threshold triggering the counter. However, one single event implies a dead time, for instance caused by the length of the produced detector signal and the electronic processing, *e.g.* the readout. Owing to this dead time the performance of counting detectors drops at high rates and dead-time corrections have to be applied to correct the measured intensities. These corrections can become complicated, particularly when counting detectors are used in synchrotron radiation facilities, owing to the intrinsic time structure of the photon beam (Bateman, 2000). The dynamic range of photon counting devices, typically reaching values of up to 10^6, is limited downwards by the number of counts owing to false triggers (noise triggers) and upwards by the (inverse) dead time. To prevent the detector from too high photon rates one has to attenuate the primary beam, and thus the full power of modern synchrotrons is wasted. Owing to the low noise level, the high dynamic range and the good time resolution, which can be approximately of the order of magnitude of the dead time or even better, single-photon counting detectors, *e.g.* one-dimensional delay-line detectors (Gabriel, 1977), are often used in SAXS imaging, for example, where only a small parallax is obtained owing to the small diffraction angles.

However, the unique detector for every application does not exist and compromises have to be found, optimizing the detector for the particular application. Although many efforts have been started to increase the readout speed of integrating CCD cameras (*e.g.* Tipnis *et al.*, 2002), the time resolution is still limited to about 1 ms. Despite their good spatial resolution and their large number of pixels, CCDs also suffer from a limited intensity precision of roughly 1% (Kocsis, 2001) and the limited dynamic range. On the other hand, single-photon counters can still not deal with the enormous rates offered by synchrotron facilities.

There are new ideas to find solutions to this drawback, *e.g.* with semiconducting pixel array detectors (Datte *et al.*, 1999; Rossi *et al.*, 1999; Renzi *et al.*, 2002). With the introduction of micropattern gaseous devices like MSGCs (Oed, 1988) or GEMs (Sauli, 1997), several new approaches have been carried out building faster gaseous detectors, *e.g.* the RAPID (refined ADC per input detector) system (Lewis, 1994; Lewis *et al.*, 1997, 2000) or a GEM pixel detector (Bellazzini *et al.*, 2001), which replace the old detector era of MWPCs. An overview of micropattern gaseous detectors can be found for example by Sauli & Sharma (1999).

The two-dimensional single-photon-counting gaseous detector for X-rays in the energy range 5–25 keV, described in this work, represents a concept which is very flexible and can therefore easily be adapted to special requirements. It offers time resolutions in the sub-µs range and is thus qualified for time-resolved SAXS imaging.

2. Detector set-up

In this section we briefly describe the working principle and the set-up of the detector. Detailed information about the detector can be found elsewhere (Besch *et al.*, 1997; Sarvestani, Besch, Junk, Meißner, Pavel *et al.*, 1998; Wagner *et al.*, 2003; Orthen, Wagner, Besch, Martoiu *et al.*, 2003). A review of a previous similar detector with a

 DOI: 10.1107/S0909049503028863

smaller sensitive detection area and a less sophisticated position reconstruction, with a different gas gain structure and with slower electronics and readout, has also been published earlier (Sarvestani, Amenitsch *et al.*, 1999).

Fig. 1 shows a schematic cross section of the detector. The X-ray photons enter the detector through the carbon-fibre entrance window and the subjacent 50 µm-thick mylar foil clad with a few µm-thick carbon layer at the bottom serving as a drift cathode. Inside the conversion region between the drift cathode and the (first) gas gain structure (gap of about 25 mm, which is a compromise between a good photoeffect efficiency and moderate parallax), one single photon produces a few hundred primary electrons in the gas volume, which is typically filled with Xe/CO_2 (90/10).

Since this charge amount is too small to be detected, additional amplification is necessary. For this purpose, micropattern devices like MicroCAT (micro compteur à trous) (Sarvestani, Besch, Junk, Meißner, Sauer *et al.*, 1998) or GEM (Sauli, 1997) have been intensively tested (Sarvestani, Besch *et al.*, 1999; Orthen, Wagner, Besch, Menk & Walenta, 2002; Orthen, Wagner, Besch, Menk *et al.*, 2003; Orthen, Wagner, Besch, Martoiu *et al.*, 2003). The MicroCAT has many advantages, such as stable gas gaining at high rates, time stability or an enormous robustness. Nevertheless, we were not successful in finding a suitable spacer concept which should guarantee a constant distance to the subjacent readout anode. Therefore, we decided not to use this device. For the GEM an external spacer concept is not necessary and, despite some disadvantages like rate- and time-dependent gas gaining which are discussed in §3, we have decided to use a constellation of three consecutive GEMs (triple-GEM).

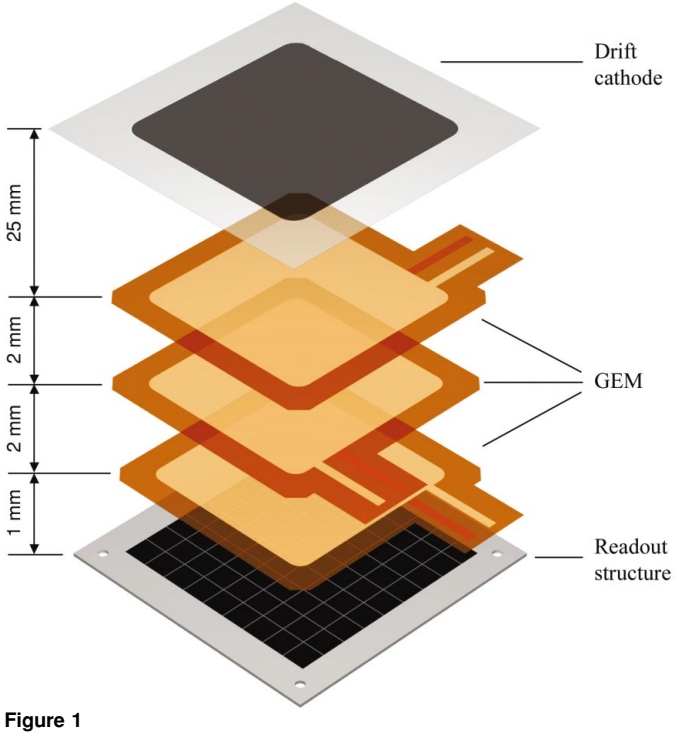

Figure 1
Schematic cross section of the triple-GEM detector set-up. The sensitive area has a size of 56 mm × 56 mm, subdivided into 7 × 7 cells (the readout structure actually contains 9 × 9 cells, whereby the outermost cells are dummy cells). The drift cathode is typically supplied with a voltage of −4000 V, in combination with the (not shown) drift cage providing a homogeneous drift field of ∼1 kV cm^{-1}. The readout structure is at ground potential. The electric field between the individual GEMs is set to 2.5 kV cm^{-1} and that between the undermost GEM and the readout structure to 3 kV cm^{-1}.

After multiplication the charge cluster hits the readout anode, which is realised by an interpolating resistive structure, where the spatial information of the event is determined in two dimensions (Besch *et al.*, 1997). The sensitive area of the readout structure is divided into 7 × 7 square cells. Each cell (Fig. 2), which has an edge length of g = 8 mm and a surface resistance of 100 kΩ/□, is surrounded by better conducting borders with a width of about 200 µm and a surface resistance of 1 kΩ/□. The resistive material is printed onto a ceramics or a printed circuit board (PCB) medium, based on FR4. The charge flows to the readout nodes at the corners of the cells, which are connected by small through connections to the back of the readout structure. By means of linear reconstruction algorithms, *e.g.* using only the collected charges Q_i at the four readout nodes of one cell (four-node algorithm), the event position can be calculated within the cell. For a proper reconstruction using combinations of several linear algorithms (four/six/three-node algorithm), nine nodes should always be read out (Wagner *et al.*, 2003).

Owing to this interpolating concept, the cells can be subdivided into virtual pixels (ViP) and a large sensitive area can be covered, simultaneously reaching a spatial resolution of the order of 100 µm (FWHM) which is almost two orders of magnitude better than the size of a cell (this spatial resolution can only be obtained in combination with adequate electronics and a gas gain of about 10^4 since the spatial resolution is directly proportional to the reciprocal signal-to-noise ratio, *i.e.* $\propto \mathrm{SNR}^{-1}$).

Each readout charge is amplified by a charge-sensitive amplifier and digitized by a 12 bit ADC (analog-to-digital converter) sampling with a frequency of 66 MHz. Four ADC channels corresponding to one detector cell are placed together at one ADC card, where they are connected to one complex Xilinx FPGA (field programmable gate array) logic device (Nurdan *et al.*, 2003). *Via* point-to-point links, the 16 ADC cards, containing all 64 channels, can communicate with their direct neighbours, while the data/control bus supports the communication with a master card, controlling the data latch to the PC (Fig. 3).

Together with the signal information, a time stamp in terms of a µs or ns counter is digitally recorded. The counter can be reset exter-

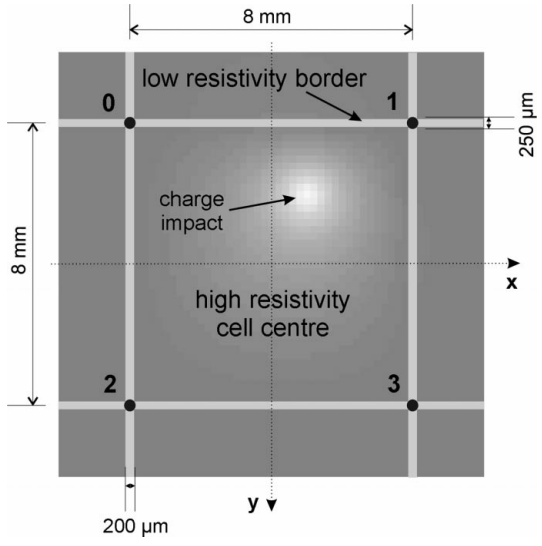

Figure 2
Schematic of one cell of the (PCB) readout structure. Around the charge impact point the electric potential increases, displayed by the white colour, and the thereby created electric field forces the charge to move towards the readout nodes at the cell corners.

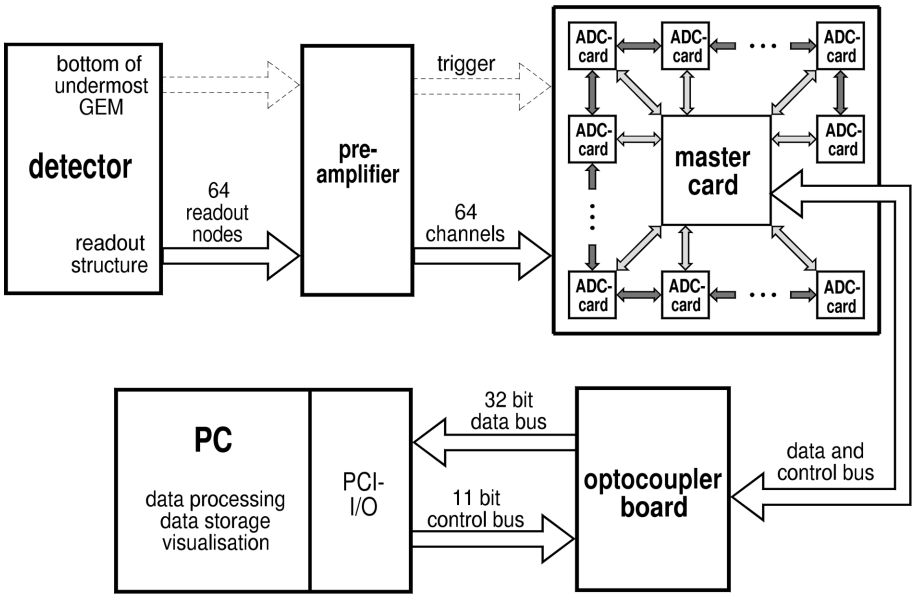

Figure 3
Block schematic of the readout.

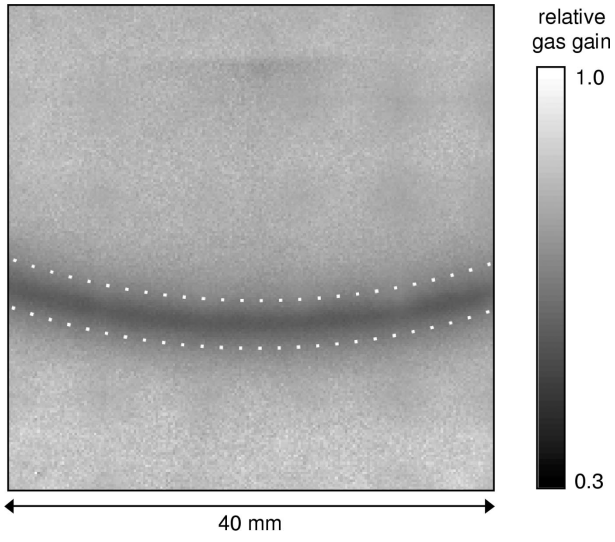

Figure 4
Relative gain in the region of the inner 5 × 5 cells of the sensitive area during the measurement of a silver behenate diffraction target. In the high rate diffraction ring area (within the white dotted lines) the photon flux is about 50 times higher than in the background; the gain drops roughly by a factor of two (dark colours).

nally. Additionally, an external signal (*e.g.* a linear ramp) can be digitized by the ADC at the master card. The time information can be used to slice the data after the measurement has been finished.

The digitized data from the ADC cards are stored in a FIFO inside the Xilinx on the master card, which is connected *via* optocouplers to a PC using a standard 32 bit PCI interface. Currently, the transfer in DMA mode can latch data with a speed of 12 MB s^{-1} into the memory of the PC. By using an alternative PCI card the transfer speed can even be increased to 80 MB s^{-1}. A dedicated software package, written in Visual C++, processes data online, so that the user is directly able to evaluate the running measurements. The raw data, as well as the already processed image histogram, can be stored to hard disk. Each event occupies 25 bytes in the raw data file.

3. Detector performance

3.1. Gas gain

Each individual GEM foil produces a gas gain of about 10–100, if the GEM operation voltage amounts to about 300–600 V depending on gas mixture and pressure. The total gas gain of a triple-GEM constellation can easily exceed 10^4 and stable operation in xenon gas mixtures up to 2×10^5 Pa at this gain is possible (Orthen, Wagner, Besch, Martoiu *et al.*, 2003). Operation with pressure $>3 \times 10^5$ Pa with high-Z gases like xenon is not advisable owing to a high discharge probability at gains $>5 \times 10^3$. The use of the triple-GEM for hard X-ray detection ($E_\gamma \gtrsim 25$ keV) is therefore rather limited.

Since the GEM technology is well sophisticated and intensively tested, large-area GEMs can also be built (Bachmann *et al.*, 2000) and thus large sensitive areas are feasible.

The gain homogeneity over the total area of the triple-GEM constellation at uniform illumination is much superior to MicroCAT detectors because no external spacer concept is needed owing to the intrinsic constant thickness of the Kapton foil and the width of the multiplication gap, respectively. Disadvantageous is the fact that the GEM can easily be destroyed by too heavy sparks. To avoid this destruction, large-area GEMs should be subdivided in order to reduce the capacitance of the individual sectors (Bachmann *et al.*, 2000, 2002). The detector should always be operated in safe voltage and gas gain ranges, if possible.

Owing to charging up of the Kapton, the gas gain drops as a function of illumination time and rate. As an example, Fig. 4 shows the measured relative gain distribution as a function of the position in the detector during the measurement of a silver behenate diffraction target with high local rates (*cf.* §4.3.2). In counting detectors, like the detector presented here, the rate- and time-dependence of the gas gain is not relevant as long as the signals do not drop below the trigger threshold. However, an energy selectivity cannot be carried out for inhomogeneous images and, owing to the decreasing signal-to-noise ratio, the spatial resolution drops in highly illuminated areas. This has to be compensated by a very high overall gas gain (which is easily possible with the triple-GEM), which requires a high dynamic range of analogue and digital electronics. Owing to the time- and rate-dependent behaviour, the GEM cannot be used as a preamplification stage in integrating systems, as planned for the MicroCAT device (Menk *et al.*, 1999). To stop the charging of the Kapton and thus to keep the gas gain rate- and time-independent, a coating of the GEM with amorphous carbon is proposed (Beirle *et al.*, 1999). The energy resolution of the triple-GEM is then expected to be of the order of 20% at 8 keV, which can also be obtained with standard (uncoated) GEMs in homogeneous illumination or single-photon spots with constant X-ray flux after an equilibrium state has been reached.

3.2. High rate capability

In counting detectors one has to make a compromise between high rate capability and spatial resolution. In general, a detector can be optimized to deal with high rates by a very fast shaping of the analogue signals, at the same time, however, losing spatial resolution

owing to too little collected charge and thus a too small SNR. The most elegant way of avoiding these problems is to produce very short intrinsic detector signals, which is a big advantage of micropattern devices in contrast to MWPCs. The GEM features a very fast signal shape at the anode, which is induced only by electrons. The $\sim 10^3$ times slower ions do not make any contribution to the signal, which is, however, the case for other micropattern devices like MicroCAT or micromegas (micromesh gaseous structure) (Giomataris *et al.*, 1996). In our detector set-up the raw anode signals have approximately a Gaussian shape with a mean length of 20–100 ns (FWHM) for Ar/CO_2 (90/10) at standard pressure and Xe/CO_2 (90/10) at a pressure of 3×10^5 Pa (Orthen, Wagner Menk, Martoiu *et al.*, 2003).

The relatively high resistance and capacitance of the sensitive area leads to an integrating RC-element-like behaviour of the readout structure, resulting in a temporal broadening of the input signal (Fig. 5). After the signal information has crossed the cell from the point of impact towards the readout nodes, the total signal width has increased.

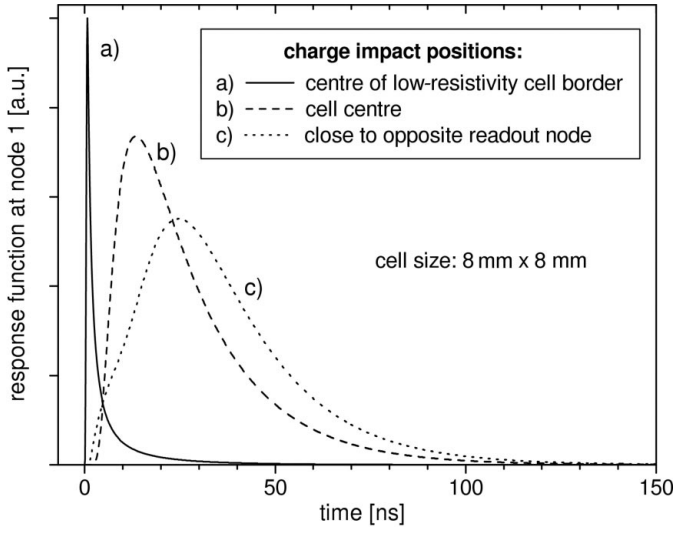

Figure 5
Simulation of the signal diffusion behaviour of the PCB-readout structure (Wagner *et al.*, 2002) for a δ-like input signal at three different charge impact positions (*cf.* Fig. 2 for node denotation): (*a*) symmetrically between node 0 and 1 on the low-resistivity cell border; (*b*) cell centre; (*c*) close to node 2. The displayed currents are read out at node 1. Since the absolute current values obtained at impact positions (*b*) and (*c*) are very small compared with those obtained at position (*a*), we scaled the plotted functions arbitrarily to increase the clarity of the figure.

Owing to the interpolating character of the image reconstruction we have to make sure that the signals do not pile up in a certain area. Affected by this constraint is, at maximum, an area of 3×3 cells containing the cell with the charge impact as the central area (Fig. 6). In this simulation the reconstruction is carried out with a simple four-node algorithm, using only the charges collected at the four central nodes. This is a worst-case estimation for two contemporaneous events. The later the second event appears within the dead-time window of the first event, the smaller is the distortion. With a typical amplified signal having a length of <100 ns, the average detected flux is limited to 10^6 photons $(3 \times 3 \text{ cells})^{-1}$ with less than 10% dead-time loss. This value corresponds to an average detected flux of about 2×10^5 photons cm^{-2} s^{-1} for a detector with a cell size of 8 mm $\times$ 8 mm, which is a true value. This means that the global count-rate capability is the product of the average detected flux and the total size of the detector. Note that, apart from pure pixel devices, a similar principle limitation in local rate capability is found for all interpolating devices, although it is often not explicitly mentioned. Often one finds a mismatch between the global rate capability and the number given for the average detected flux multiplied by the active area of the detector. This is not the case for the numbers given in this work.

Since the arising dead area is always measured in cell units, a decrease in cell size leads to a higher average detected photon rate per unit area. By decreasing the cell size, for instance, to 2 mm $\times$ 2 mm, the average detected flux increases by a factor of 16 to $>3 \times 10^6$ photons cm^{-2} s^{-1}. In principle, one is free to adapt the cell size to be able to deal with the desired photon rates. However, the cell size is limited upwards by the deteriorating spatial resolution and the signal diffusion, which increases almost proportionally to the square of the cell edge length, g^2 [this result was obtained by simulations (Wagner, 2004)]. Decreasing the cell size is limited by the readout speed of the electronics, which cannot be exceeded. Moreover, if the cell size is chosen too small (<1 mm $\times$ 1 mm), the advantage of the interpolating readout system vanishes; in this case a pure pixel device is much more advantageous and easier to handle. By means of a complex signal recognition, double events may potentially be

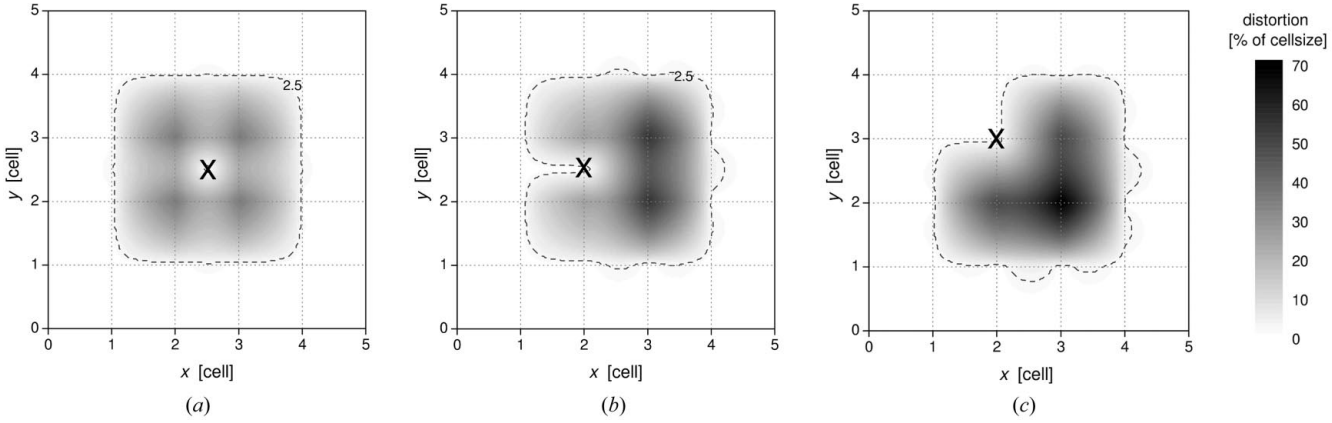

Figure 6
Worst-case estimation of the reconstruction distortions (in percent of the cellsize), appearing at two contemporaneous events. The X marks the impact position of the first event for which the distortion is determined: (*a*) in the cell centre; (*b*) at the centre of a low-resistivity cell border; (*c*) at a node. The absolute value of the expected distortions on the position of the first event X are plotted as a function of the impact position of the second event. The dashed contour lines correspond to a distortion of 2.5% of the cell size, *i.e.* 200 µm for a cell size of g = 8 mm. The ratio between high-resistivity cell centre and low-resistivity cell border amounts to 100.

processed properly in future, which would improve the local rate capability enormously. As yet, this feature has not been investigated.

Another rather critical point in gaseous avalanche detectors is the influence of space charge produced by the multiplication process, mainly of the slowly drifting ions, causing spatial reconstruction distortions, because the electrons, drifting from the conversion gap towards the gain regions, are attracted by the ion space charge. A big advantage of micropattern devices compared with, for example, MWPCs, is the fact that the amount of ions, drifting back from the multiplication regions to the drift cathode, is relatively small. In the case of the triple-GEM we have measured an ion feedback <5% (Orthen, 2004). With special care in choosing the parameters of the GEM it should be possible to suppress the ion feedback to less than 3% at a gain of 10^4 (Breskin *et al.*, 2002; Bondar *et al.*, 2003), but this has still to be proven experimentally. For the MicroCAT in combination with the resistive readout structure we have measured no serious degradation in operation owing to space charge at photon peak fluxes $>10^7$ photons mm^{-2} s^{-1} with a beam collimation of $\lesssim 0.1\ mm^2$. Also, the GEM can work with high local fluxes (Östling *et al.*, 2003).

3.3. Noise level and intensity precision

The noise level of the triple-GEM detector is around a few counts per second over all the sensitive area, typical for counting detectors. For a 280 × 280 virtual pixel interpolation, corresponding to a pixel size of 200 µm × 200 µm, the noise level is far below 10^{-4} counts s^{-1} $pixel^{-1}$. Intensity precision is thus, as expected, only Poisson-limited and can be better than 0.1%.

3.4. Analogue electronics

The charge integrating preamplifiers with subsequent shaping, currently in use, have a shaping time of 300 ns. They have not been optimized for this application, but were rather built for a MWPC which produces signals with long ion tails. In the future we plan to use a linear transimpedance preamplifier. The charge collection by current integration can be carried out digitally afterwards in the FPGA. One prototype channel which has already been tested responds to a δ-like input with a Gaussian signal shape with a width of about 15 ns (FWHM) owing to bandwidth limitations.

3.5. Preprocessing and data readout

The data readout crucially influences the dead-time behaviour of the overall system. In a previous version of the electronics (Stiehler *et al.*, 1998) the data transfer used to be the bottleneck of the readout, which limited the readout speed dramatically and implied additionally an electronic dead time of about 10 µs per event. The synchronous readout was triggered by an externally generated signal ('global trigger') which was created by the discriminated signal from the bottom of the lowermost GEM (or from the MicroCAT, respectively).

The newly developed very modular ADC system enables a parallel and asynchronous readout of the nine nodes of interest, carrying the most important information of one event. Furthermore, it offers the capability of preprocessing before data are latched to the PC. The processing is performed by Xilinx FPGA devices which are freely programmable using a hardware description language like VHDL. The new system is, for example, able to integrate the current signal, to find the signal peak and to locate the node with the maximum signal and the surrounding eight nodes autonomously. Furthermore, it can work in a self-triggering mode, *i.e.* a trigger is generated by a signal-recognition unit. This trigger signal need not serve as a global trigger but rather as a 'local' trigger which means that only the region of interest is triggered for readout while the neighbouring channels (at least two cells away) are not read out and thus work in a normal fashion. During the readout of the nine nodes of interest the participating ADC channels are continuously sampling new data, so that no additional dead time occurs. For the final version of the local trigger programming we expect that the dead-time contribution due to the readout is small compared with the signal lengths (Martoiu *et al.*, 2003).

Owing to the modularity, an upgrade to a larger system can be realised by a replication of the system described above. The master cards of these subsystems have to be connected to an overall master. Thereby, it should be possible to extend the detector by scaling the sensitive area and the global rate capability at the same time without loss of spatial resolution and local rate capability. When the number of electronic channels exceeds a certain limit, the whole reconstruction work should be implemented in the FPGA logic devices on the system master card(s) by making use of the newest generation of FPGAs featuring fast multiplier/divider units. By only transmitting the (already time-sliced) histograms instead of the raw data, the data transfer to the PC will be compressed by several orders of magnitude.

Unfortunately, the measurements, described in this publication, could only be carried out using a 'slim' version, which meant that the Xilinx devices were programmed with a less complex test mode VHDL programme. It is still based on a global trigger which is distributed to the whole system by one dedicated ADC channel, that originally used to digitize data at the corner of the sensitive area (*cf.* the black dead area in the lower right-hand corner of Fig. 10). After the trigger has been received by the other ADC cards, the peak sampling point in a defined time window of each channel is transmitted to the master card that decides which nine nodes are sent to the PC. The dead time of this procedure amounts to about 4 µs. The local trigger programming is currently under development, and a simple prototype version has already been tested successfully.

3.6. Time resolution

With the triple-GEM detector and the new digital (and analogue) electronics it seems sensibly feasible to reach continuous time resolutions in the 100 ns range; thereby, the time resolution is limited by the width of the conversion gap d_{gap}: incoming photons may convert into electrons by the photoeffect everywhere in this gap (actually more photons convert directly behind the entrance window compared with positions directly above the GEM owing to the exponential absorption law). By this physical process the time resolution is limited by the maximum electron drift time, $\tau_{max} = d_{gap}/v_e$, in the conversion gap. Typical values for the electron drift velocity are v_e = 3–4 cm μs^{-1} in xenon-based gas mixtures at standard pressure (Becker *et al.*, 1999). This means that the time resolution is limited to about 800 ns for a 25 mm conversion gap. The drift gap can be chosen smaller, at the same time losing quantum efficiency. Increasing the gas pressure to increase efficiency will decrease drift velocity and hence increase the drift time. Maybe the addition of CF_4 to the xenon mixture can increase the electron drift velocity (Va'vra *et al.*, 1993). Simulations with the *Magboltz* programme show promising results (Biagi, 1999).

The limitation of the time resolution, described above, is actually similar in all gaseous devices where a larger conversion gap is needed to gain sufficient quantum efficiency. Incidentally, the timing structure of the synchrotron beam caused by the individual electron bunches in the storage ring is also lost due to the slower electron drift in the conversion gap; for ELETTRA or ESRF the minimum time

difference between two bunches (with uniform bunch pattern) amounts to about 2 ns.

4. Imaging performance

The images, shown in the following subsections, have been recorded with two different readout structures based either on a ceramics or on a PCB. Both substrates have advantages and disadvantages, as follows.

The AlO_2 ceramic medium is very planar and therefore well suited for operation with a MicroCAT gas gain structure. However, it suffers from a high dielectric constant (ε = 9.9 @ 1 MHz) leading to a large capacitance of the resistive area and therefore to a large signal diffusion at the readout structure (*cf.* §3.2). Furthermore, the through-contacts have a relatively large diameter of 300–400 µm, leading to image distortions in the surrounding area of the nodes.

The newly introduced PCB structure is not planar and hence not suited in combination with the MicroCAT without a sophisticated spacer concept. In combination with the triple-GEM, however, the advantages outbalance the ceramics owing to the lower dielectric constant (ε = 4.6 @ 1 MHz), the possibility of using micro-vias at the readout nodes with a diameter of only 200 µm, and the very flexible multilayer configuration.

4.1. Flatfield response

Owing to a slightly non-linear behaviour of the ViP readout structure it is not possible to reconstruct distortion-free images with only one linear algorithm. Fig. 7(*a*) shows the response of a detector with a PCB-readout structure to a uniform illumination reconstructed with a simple four-node algorithm. A ^{55}Fe source has been used for illumination (E_γ = 5.9 keV). The detector has been operated with an Ar/CO_2 (70/30) gas filling at a pressure of 1.2×10^5 Pa. The depletion at the cell border shows the non-linear charge division behaviour. By using a more complex linear four/six/three-node algorithm (Wagner *et al.*, 2003), these kinds of distortions do not occur anymore (Fig. 7*b*). However, the population density is still not as flat as it should be (*i.e.* the nodes are overpopulated) owing to systematic effects like cross talk, electronic gain variations,† variations of the resistance of the sensitive area or the width of the low-resistivity cell borders or simply signal fluctuations owing to noise (Wagner, 2004). To further improve the image, one can apply a non-linear correction (two-dimensional variable transformation), resulting in the image shown in Fig. 7(*c*). All further images have been reconstructed with the linear four/six/three-node algorithm with a global non-linear correction at the nodes and at the cell borders.

4.2. Aperture image

4.2.1. Hole grid collimator. An image of a hole grid collimator consisting of a stainless steel aperture with 0.5 mm-diameter holes at a grid distance of 8 mm is depicted in Fig. 8. It becomes obvious that close to the border of the detector the image is slightly distorted. These distortions are mainly caused by a slightly inhomogeneous drift field and can be avoided by the use of an additional electrode frame which is fixed upon the ceramic frame, holding the uppermost GEM. Distortions owing to field inhomogeneities can also be caused by inhomogeneous electric fields between the individual GEMs (transfer field) and between undermost GEM and readout structure (induction field). It is very important that the distance between the individual electrodes is as constant as possible. In particular, the transfer and

† Gas gain variations displace the event position only far less than the value of the spatial resolution (Orthen, 2000).

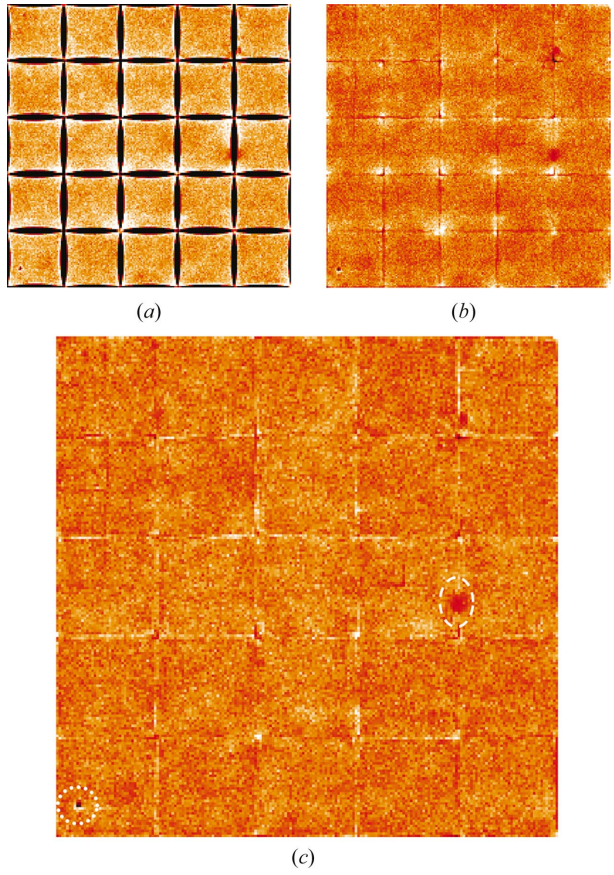

Figure 7
Reconstructed image of a flatfield illumination using (*a*) the simple four-node algorithm, (*b*) the four/six/three-node algorithm and (*c*) the four/six/three-node algorithm with subsequent non-linear correction mainly at the nodes and the cell borders. The flatfield shown has been recorded with a PCB-readout structure. Only the inner 5 × 5 cells corresponding to an area of 40 mm × 40 mm are depicted. A virtual pixel size of 200 µm × 200 µm has been chosen. All images contain about 4.6×10^6 photons (mean number of photons per pixel $N \simeq 114$). The standard deviation of the intensity per pixel distribution amounts to σ_N = 54.9 in image (*a*), to σ_N = 16.2 in image (*b*) and to σ_N = 13.6 in image (*c*). The Poisson limit amounts to $\sigma_{\text{N-Poisson}} = 114^{1/2} \simeq 10.7$. The black spot in the lower left-hand area (dotted circle) is caused by a defect region in one of the three GEM structures. The larger dark grey spot in the right-hand half of the image (dashed ellipse) can be attributed to an irregularity of the low-resistivity cell border.

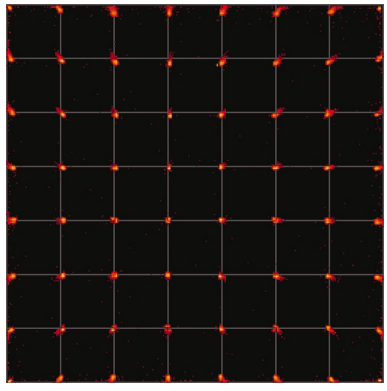

Figure 8
Image of a hole grid collimator, recorded with a PCB-readout structure. A ^{55}Fe source has been placed at a distance of 30 cm in front of the detector, causing visible parallax. The detector has been operated at a pressure of 1.2×10^5 Pa Xe/CO_2 (90/10) with an applied drift field of 1 kV cm^{-1}.

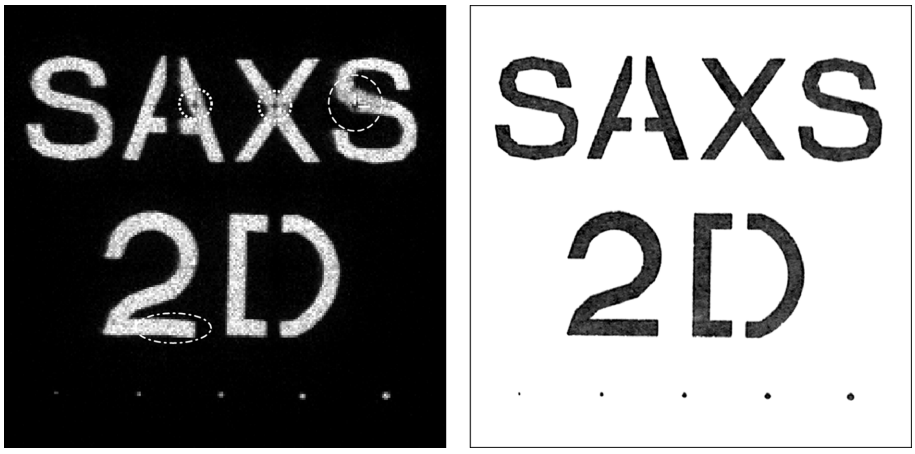

Figure 9
Image of the 'SAXS' aperture recorded with the ViP detector (left-hand side) and photograph taken with a standard digital camera against the sunlight (right-hand side). The detector image has been recorded with a beam energy of 6.4 keV. The distance between detector and source amounted to about 2.5 m, therefore parallax is small. The illuminated spots at the bottom correspond to holes in the aperture with diameters of 280, 380, 480, 580 and 680 µm. The aperture is slightly tilted by an angle of about 0.6°, which can be recognized for example by the vertical pixel jump at the bottom of the '2' (dashed-dotted ellipse). The sizes of both depicted images amount to 4.4 cm × 4.4 cm. Note that the cell borders have almost disappeared.

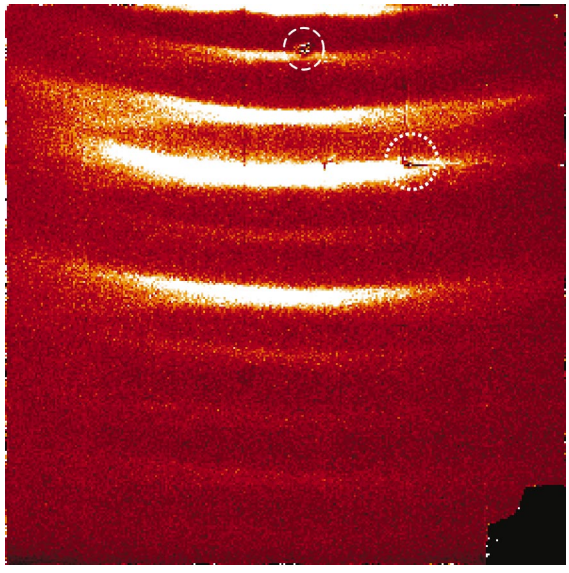

Figure 10
Diffraction image of a rat tail tendon, recorded with a ceramic readout structure. The image size amounts to 56 mm × 56 mm. The node at the lower right-hand image corner was used for triggering and therefore caused a black dead area. The distorted spot in the second visible diffraction order (actually the 7th diffraction order) is caused by a defect region in one of the GEM structures (dashed circle). The region of the problematic preamplifier channel is marked with a dotted circle. The image has been flatfield-corrected with a non-optimized flatfield image.

induction fields are very sensitive to these variations owing to the small distance of 1–2 mm of the particular electrodes. Transfer and induction field variations are also a possible reason for global gas gain variations because the effective gas gain is determined by the electron transfer through the GEM holes which is strongly affected by the electric fields close to the GEM structures (Orthen, Wagner, Besch, Menk *et al.*, 2003).

4.2.2. SAXS collimator. Fig. 9 shows an image of a laser-cut 1 mm-thick stainless steel aperture containing the letters 'SAXS 2D' and five holes of increasing diameters. The image has been recorded with a PCB-readout structure using photons of an energy of 6.4 keV (fluorescence of a Fe target in a 8 keV synchrotron beam). The detector was filled with a Xe/CO_2 (90/10) gas mixture at a pressure of 1.3×10^5 Pa. The comparison with a photographic image of the aperture (right-hand side image in Fig. 9) shows a very good accordance. Only the middle part of the second 'S' (dashed circle) looks slightly distorted; at this readout channel the preamplifier was not working fully correctly and caused slight distortions in all images shown. The reproduction of the small holes shows a good agreement too. The remaining spots (dotted circles) are most likely due to a non-optimized flatfield correction. Using the image of the smallest hole of the SAXS aperture with a diameter of 280 µm we have determined the width of the point spread function (PSF) to be of the order of $\sigma_{PSF} \simeq 120$ µm (FWHM).

4.3. Diffraction measurement

All diffraction patterns, presented in the following, have been recorded at the Austrian SAXS beamline (Amenitsch *et al.*, 1998; Bernstorff *et al.*, 1998) at the synchrotron ELETTRA/Trieste.

4.3.1. Rat tail tendon collagen. Fig. 10 shows a diffraction pattern of a rat tail tendon with a *d*-spacing of about 650 Å which was used for the detector calibration/alignment for the time-resolved SAXS measurements described in §5. The image has been recorded with a ceramic readout structure and a beam energy of 8 keV; the remaining detector parameters were the same as described in §4.2.2. The vertical intensity profile is shown in Fig. 11. Even the 14th and 15th diffraction order are slightly visible.

4.3.2. Silver behenate. Another standard diffraction target in the small-angle region, silver behenate $[CH_3(CH_2)_{20}–COOAg]$, with a *d*-spacing of $d_{001} = 58.38$ Å (Blanton *et al.*, 1995), has also been

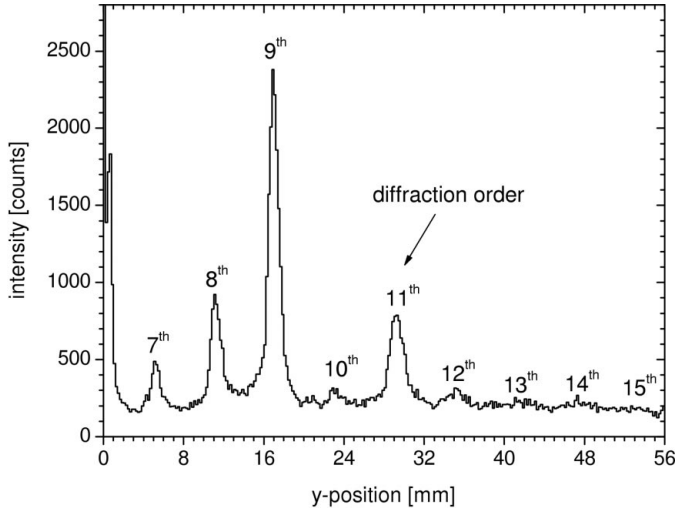

Figure 11
Intensity profile of the rat tail tendon image. Five pixels in the *x*-direction have been summed.

recorded with the ViP detector system. The image, composed of 1 × 4 individual images, is shown in Fig. 12.

5. Time-resolved SAXS

Several mechanical test measurements in our laboratory have been carried out with an X-ray tube showing the capability of the detector system to resolve very fast repetitive processes up to the µs regime (Sarvestani *et al.*, 2001). Since a slower electronic system has been used for these measurements, the processes had to be periodically repeated a few hundred or even a few thousand times in order to collect sufficient statistics. A repetition is no problem at radiation-stable materials which have been used for these measurements. However, the number of repetitions in, for example, biological X-ray diffraction measurements is limited owing to severe radiation damage of the sample.

Here we present a time-resolved temperature-jump experiment of a 1-palmitoyl-2-oleoyl-*sn*-phosphatidylethanolamine (POPE) lipid. The sample preparation is described elsewhere (Rappolt *et al.*, 2003). The sample has been placed inside a thin-walled quartz capillary with a diameter of 1 mm. The *T*-jump has been induced by a light flash from a solid-state laser at a wavelength of 1540 nm with erbium in glass as the active laser medium (Rapp & Goody, 1991). We have repeated the experiment about ten times, which was sufficient owing to the high scattering power of the sample and since we were not interested in intensity resolution but rather in the change of the *d*-spacing in the lipid owing to the rapid temperature increase, manifested by a spatial displacement of the diffraction ring.

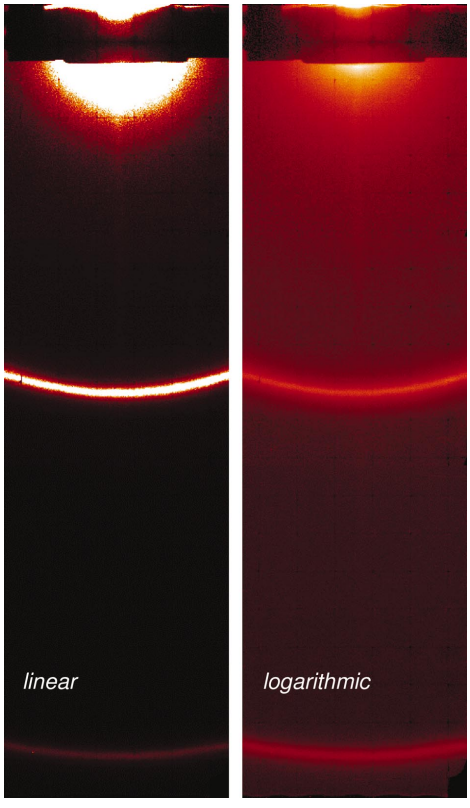

Figure 12
1 × 4 scan of a silver behenate diffraction image both with linear and logarithmic scaling. The composed image has a size of 48 mm × 168 mm. Each single image, used for the composition, has been recorded with a PCB-readout structure and flatfield-corrected with a non-optimized flatfield image.

A sketch of the experimental set-up is depicted in Fig. 13. The prepared lipid sample in a capillary device has been mounted at the intersection point of the infrared laser beam and the monochromatic 8 keV X-ray beam. A water-based cooling system combined with a heater (KHR, Anton Paar, Graz, Austria) assured a constant starting temperature of the sample which can be chosen within a temperature range of 273–423 K. The sample temperature has been measured with a PT-100 platinum resistor. Before the *T*-jump, the sample was equilibrated for a period of about 10 min at a fixed temperature. The flash-like laser pulse with a length of 2 ms and a measured pulse energy of 0.64 J appears about 1 ms after the trigger pulse and heats the sample very rapidly by approximately 5 K. We have collected data for a period of up to 30 s starting about 1 s before triggering of the laser pulse.

After the measurement the data have been cut into fine time slices (*e.g.* 3 ms slices for $0 \leq t \leq 60$ ms, where t denotes the time after the laser trigger). For the data analysis we have carried out a radial integration of the two-dimensional intensity histogram (the rat tail

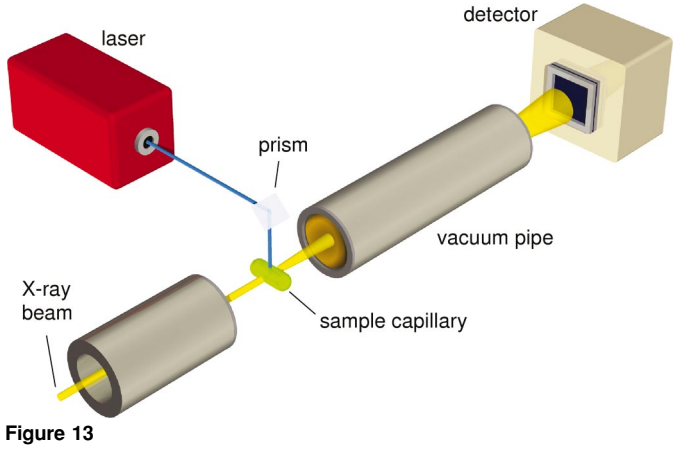

Figure 13
Schematic set-up of the *T*-jump experiment at the SAXS beamline.

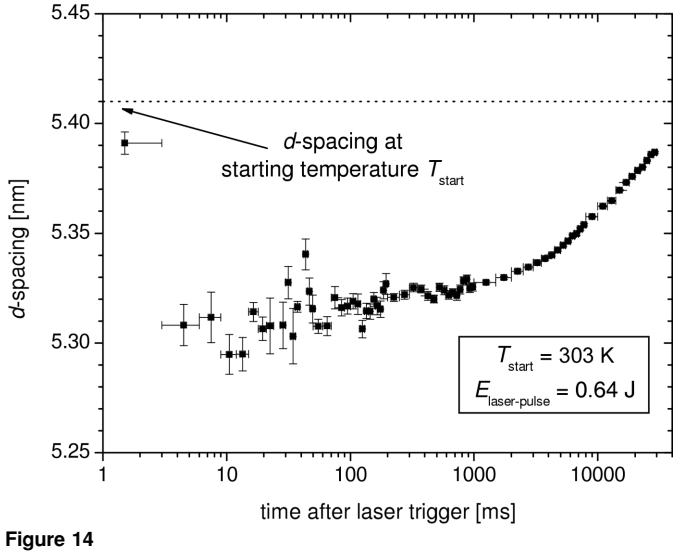

Figure 14
Measured *d*-spacing of the POPE lipid up to 30 s after the trigger of the laser pulse (at $t = 0$). The applied time slices have variable widths to give an overview over four orders of magnitude in time. The bars in the *t*-direction mark the slice-windows. Very fine 3 ms slices directly after the laser trigger show that the maximum change in *d*-spacing (and hence the maximum temperature change) occurs immediately after the end of the laser pulse (*i.e.* 3–30 ms).

Table 1
Specification of the present and a possible future ViP detector and comparison with the RAPID system (Lewis *et al.*, 1997, 2000).

	ViP (present)	ViP (future)	RAPID
Detector type	Triple-GEM	Triple-GEM	Wire microgap
Active area	5.6 cm × 5.6 cm	20 cm × 20 cm	20 cm × 20 cm
Number of cells	7 × 7	50 × 50	–
Cell size	8 mm × 8 mm	4 mm × 4 mm	–
Detected peak flux	$>10^7$ photons mm^{-2} s^{-1}	$>10^7$ photons mm^{-2} s^{-1}	$>10^6$ photons mm^{-2} s^{-1}
Average detected flux	$>2 \times 10^5$ photons cm^{-2} s^{-1}	$>8 \times 10^5$ photons cm^{-2} s^{-1}	$>4 \times 10^4$ photons cm^{-2} s^{-1}
Global counting rate	$>10^6$ photons s^{-1}†‡	$>3 \times 10^8$ photons s^{-1}†	$>1.5 \times 10^7$ photons s^{-1}§
Gas filling	1.3×10^5 Pa Xe/CO_2	2×10^5 Pa Xe/CO_2/CF_4	Xe/Ar/CO_2
Conversion gap	25 mm	8 mm	15 mm
Efficiency @ 8 keV	99%	90%	70%
Number of pixels	280 × 280¶	2000 × 2000¶	1024 × 1024¶
Number of electronic channels	8 × 8	50 × 50	128 × 128
Spatial resolution	< 150 µm FWHM	< 100 µm FWHM	∼ 300 µm FWHM
Noise level	∼ 2.5×10^{-4} counts mm^{-2} s^{-1}	∼ 2.5×10^{-4} counts mm^{-2} s^{-1}	∼ 2.5×10^{-4} counts mm^{-2} s^{-1}
Time resolution	< 600 ns††	< 250 ns††	10 ms‡‡
Spectral resolution @ 8 keV	Sufficient for triggering	20%§§	20%

† Average detected flux multiplied by detector area (proportional by design). ‡ Currently limited by global trigger technique. § Independent of size. ¶ The number of pixels can be adjusted in interpolating systems. The given values are typical pixel numbers. †† Limited by drift time. ‡‡ Limited by memory organization. §§ Expected with coating of the GEMs.

tendon image was used for the determination of the beam centre at the detector) and a subsequent Lorentzian maximum-likelihood fit to the peak. The result of the reconstructed lipid *d*-spacing as a function of time after the laser trigger of one recorded *T*-jump is shown in Fig. 14. It is clearly visible that the temperature increase of the lipid features a decrease in *d*-spacing. More detailed results concerning the *T*-jump of the POPE lipid will be published later.

6. Conclusion

The GEM-based ViP photon-counting prototype detector represents a powerful tool for time-resolved X-ray imaging applications in the ms or even the µs range (Sarvestani *et al.*, 2001). The most important parameters are summarized in Table 1, where a possible future version of the detector and a comparison with the RAPID detector are also listed. Large sensitive detection areas in combination with spatial resolution of the order of 100 µm are feasible with the virtual pixel readout concept, at the same time saving expenses owing to an enormous reduction of electronic channels. Since the GEM produces short signals, the detector can deal with high local rates without signal pile-up; average detected fluxes of $>2 \times 10^5$ photons cm^{-2} s^{-1} with less than 10% dead-time losses are easily possible. The rejection of multiple events in an area of approximately 3 × 3 cells around the position of the photon impact could possibly be overcome in future by a more complex signal processing. It is expected that the electronic local trigger concept, enabling an asynchronous readout, will be capable of dealing with very high rates so that the global rate capability is proportional to the number of cells and the sensitive area, respectively; nevertheless, this has still to be tested. The ViP detector offers a high quantum efficiency and a relatively good parallax suppression even for higher photon energies up to about 25 keV since operation at pressures up to 2–3 × 10^5 Pa in xenon mixtures is possible. The overall time resolution, which is mainly determined by the electron drift time in the conversion gap, is at a minimum of the order of a few 100 ns and thus in the sub-µs range.

We gratefully acknowledge the help of D. Junge who assisted in equipping the new electronics. We thank the inner tracker group of the HERA-B collaboration for providing several GEM foils. This work has been supported by the European Community (contract No. ERBFMGECT980104).

References

Amenitsch, H., Rappolt, M., Kriechbaum, M., Mio, H., Laggner, P. & Bernstorff, S. (1998). *J. Synchrotron Rad.* **5**, 506–508.
Bachmann, S., Bressan, A., Capeáns, M., Deutel, M., Kappler, S., Ketzer, B., Polouektov, A., Ropelewski, L., Sauli, F., Schulte, E., Shekhtman, L. & Sokolov, A. (2002). *Nucl. Instrum. Methods*, A**479**, 294–308.
Bachmann, S., Bressan, A., Placci, A., Ropelewski, L. & Sauli, F. (2000). *IEEE Trans. Nucl. Sci.* **47**, 1412–1415.
Bateman, J. E. (2000). *J. Synchrotron Rad.* **7**, 307–312.
Becker, U., Dinner, R., Fortunato, E., Kirchner, J., Rosera, K. & Uchida, Y. (1999). *Nucl. Instrum. Methods*, A**421**, 54–59.
Beirle, S., Werthenbach, U., Zech, G. & Zeuner, T. (1999). *Nucl. Instrum. Methods*, A**423**, 297–302.
Bellazzini, R., Brez, A., Gariano, G., Latronico, L., Lumb, N., Spandre, G., Massai, M. M., Reale, S., Pacella, D., Pizzicaroli, G., Gaballieri, L. & Leigheb, M. (2001). *Rev. Sci. Instrum.* **72**, 1372–1378.
Bernstorff, S., Amenitsch, H. & Laggner, P. (1998). *J. Synchrotron Rad.* **5**, 1215–1221.
Besch, H. J., Junk, M., Meißner, W., Sarvestani, A., Stiehler, R. & Walenta, A. H. (1997). *Nucl. Instrum. Methods*, A**392**, 244–248.
Biagi, S. F. (1999). *Nucl. Instrum. Methods*, A**421**, 234–240.
Blanton, T. N., Huang, T. C., Toraya, H., Hubbard, C. R., Robie, S. B., Louër, D., Göbel, H. E., Will, G., Gilles, R. & Raftery, T. (1995). *Powder Diffr.* **10**, 91–95.
Bondar, A., Buzulutskov, A., Shekhtman, L. & Vasiljev, A. (2003). *Nucl. Instrum. Methods*, A**496**, 325–332.
Breskin, A., Buzulutskov, A., Chechik, R., Singh, B. K., Bondar, A. & Shekhtman, L. (2002). *Nucl. Instrum. Methods*, A**478**, 225–229.
Clery, D. (1997). *Science*, **277**, 1213–1253.
Datte, P., Birkbeck, A., Beuville, E., Endres, N., Druillole, F., Luo, L., Millaud, J. & Xuong, N.-H. (1999). *Nucl. Instrum. Methods*, A**421**, 576–590.
Gabriel, A. (1977). *Rev. Sci. Instrum.* **48**, 1303–1305.
Giomataris, Y., Rebourgeard, Ph., Robert, J. P. & Charpak, G. (1996). *Nucl. Instrum. Methods*, A**376**, 29–35.
Holmes, K. C. & Geeves, M. A. (2000). *Philos. Trans. R. Soc. London*, B**355**, 419–431.
Kocsis, M. (2001). *Nucl. Instrum. Methods*, A**471**, 103–108.
Lewis, R. (1994). *J. Synchrotron Rad.* **1**, 43–53.
Lewis, R. A., Berry, A., Hall, C. J., Helsby, W. I. & Parker, B. T. (2000). *Nucl. Instrum. Methods*, A**454**, 165–172.

Lewis, R. A., Helsby, W. I., Jones, A. O., Hall, C. J., Parker, B., Sheldon, J., Clifford, P., Hillen, M., Sumner, I., Fore, N. S., Jones, R. W. M. & Roberts, K. M. (1997). *Nucl. Instrum. Methods*, A**392**, 32–41.
Martoiu, S., Orthen, A., Wagner, H., Besch, H. J., Menk, R. H., Nurdan, K., Walenta, A. H. & Werthenbach, U. (2004). *Nucl. Instrum. Methods.* To be published.
Menk, R. H., Arfelli, F., Bernstorff, S., Pontoni, D., Sarvestani, A., Besch, H. J. & Walenta, A. H. (1999). *Nucl. Instrum. Methods*, A**422**, 698–703.
Nurdan, K., Çonka-Nurdan, T., Besch, H.-J., Freisleben, B., Pavel, N. A. & Walenta, A. H. (2003). *Nucl. Instrum. Methods*, A**510**, 122–125.
Oed, A. (1988). *Nucl. Instrum. Methods*, A**263**, 351–359.
Orthen, A. (2000). Master's thesis, Siegen University, Germany.
Orthen, A. (2004). PhD thesis, Siegen University, Germany.
Orthen, A., Wagner, H., Besch, H. J., Martoiu, S., Menk, R. H., Walenta, A. H. & Werthenbach, U. (2003). *Nucl. Instrum. Methods*, A**512**, 476–487.
Orthen, A., Wagner, H., Besch, H. J., Menk, R. H. & Walenta, A. H. (2002). *Nucl. Instrum. Methods*, A**492**, 160–177.
Orthen, A., Wagner, H., Besch, H. J., Menk, R. H., Walenta, A. H. & Werthenbach, U. (2003). *Nucl. Instrum. Methods*, A**500**, 163–177.
Östling, J., Brahme, A., Danielsson, M., Francke, T., Iacobaeus, C. & Peskov, P. (2003). *IEEE Trans. Nucl. Sci.* NS**50**, 809–819.
Piazzesi, G., Reconditi, M., Linari, M., Lucii, L., Sun, Y. B., Narayanan, T., Boesecke, P., Lombardi, V. & Irving, M. (2002). *Nature (London)*, **415**, 659–662.
Rapp, G. (1991). *Proceedings of the European Workshop on X-ray Detectors for Synchrotron Radiation Sources*, Aussois, France, pp. 72–75. Sigen, Germany: Zess.
Rapp, G. & Goody, R. S. (1991). *J. Appl. Cryst.* **24**, 857–865.
Rappolt, M., Hickel, A., Bringezu, F. & Lohner, K. (2003). *Biophys. J.* **84**, 3111–3122.
Renzi, M. J., Tate, M. W., Ercan, A., Gruner, S. M., Fontes, E., Powell, C. F., MacPhee, A. G., Narayanan, S., Wang, J., Yue, Y. & Cuenca, R. (2002). *Rev. Sci. Instrum.* **73**, 1621–1624.
Rossi, G., Renzi, M., Eikenberry, E. F., Tate, M. W., Bilderback, D., Fontes, E., Wixted, R., Barna, S. & Gruner, S. M. (1999). *J. Synchrotron Rad.* **6**, 1096–1105.
Sarvestani, A., Amenitsch, H., Bernstorff, S., Besch, H.-J., Menk, R. H., Orthen, A., Pavel, N., Rappolt, M., Sauer, N. & Walenta, A. H. (1999). *J. Synchrotron Rad.* **6**, 985–994.
Sarvestani, A., Besch, H. J., Junk, M., Meißner, W., Pavel, N., Sauer, N., Stiehler, R., Walenta, A. H. & Menk, R. H. (1998). *Nucl. Instrum. Methods*, A**419**, 444–451.
Sarvestani, A., Besch, H. J., Junk, M., Meißner, W., Sauer, N., Stiehler, R., Walenta, A. H. & Menk, R. H. (1998). *Nucl. Instrum. Methods*, A**410**, 238–258.
Sarvestani, A., Besch, H. J., Menk, R. H., Pavel, N., Sauer, N., Strietzel, C. & Walenta, A. H. (1999). *Nucl. Phys. B (Proc. Suppl.)*, **78**, 431–437.
Sarvestani, A., Sauer, N., Strietzel, C., Besch, H. J., Orthen, A., Pavel, N., Walenta, A. H. & Menk, R. H. (2001). *Nucl. Instrum. Methods*, A**465**, 354–364.
Sauli, F. (1997). *Nucl. Instrum. Methods*, A**386**, 531–534.
Sauli, F. & Sharma, A. (1999). *Ann. Rev. Nucl. Part. Sci.* **49**, 341–388.
Seddon, J. & Templer, R. H. (1995). *Handbook of Biological Physics – Structure and Dynamics of Membranes*, Vol. 1, edited by R. Lipowsky & E. Sackmann, pp. 97–160. Amsterdam: Elsevier Science.
Squire, J. M., Harford, J. J., Chew, M. W. K. & Barry, J. (1991). *Nucl. Instrum. Methods*, A**310**, 349–353.
Stiehler, R., Adamek, M., Besch, H. J., Junk, M., Menzel, G., Neuser, E., Meißner, W., Pavel, N., Sarvestani, A., Sauer, N., Volkov, S. & Walenta, A. H. (1998). *Nucl. Instrum. Methods*, A**419**, 711–714.
Tipnis, S. V., Nagarkar, V. V., Gaysinskiy, V., Miller, S. R. & Shestakova, I. (2002). *IEEE Trans. Nucl. Sci.* **49**, 2415–2419.
Va'vra, J., Coyle, P., Kadyk, J. & Wise, J. (1993). *Nucl. Instrum. Methods*, A**324**, 113–126.
Wagner, H. (2004). PhD thesis, Siegen University, Germany.
Wagner, H., Besch, H. J., Menk, R. H., Orthen, A., Sarvestani, A., Walenta, A. H. & Walliser, H. (2002). *Nucl. Instrum. Methods*, A**482**, 334–346.
Wagner, H., Orthen, A., Besch, H. J., Menk, R. H., Walenta, A. H. & Werthenbach, U. (2004). *Nucl. Instrum. Methods.* In the press.
Wakabayashi, K. & Amemiya, Y. (1991). *Handbook on Synchrotron Radiation*, Vol. 4, edited by S. Ebashi, M. Koch & E. Rubenstein, pp. 597–678. Amsterdam: Elsevier Science.

 Received 27 October 2003 • Accepted 15 December 2003